

# Retrieval of short ocean wave slope using polarimetric imaging

Christopher J Zappa<sup>1</sup>, Michael L Banner<sup>1,2</sup>, Howard Schultz<sup>3</sup>,  
Andres Corrada-Emmanuel<sup>4</sup>, Lawrence B Wolff<sup>5</sup> and Jacob Yalcin<sup>5</sup>

<sup>1</sup> Lamont-Doherty Earth Observatory, Columbia University, 61 Route 9W, Palisades, NY 10964, USA

<sup>2</sup> School of Mathematics and Statistics, The University of New South Wales, Sydney 2052, Australia

<sup>3</sup> Department of Computer Science, University of Massachusetts, Amherst, MA 01003, USA

<sup>4</sup> Physics Department, University of Massachusetts, Amherst, MA 01003, USA

<sup>5</sup> Equinox Corporation, 9 West 57th Street, Suite 1650, New York, NY 10019, USA

E-mail: [zappa@ldeo.columbia.edu](mailto:zappa@ldeo.columbia.edu)

Received 11 October 2007, in final form 19 March 2008

Published 21 April 2008

Online at [stacks.iop.org/MST/19/055503](http://stacks.iop.org/MST/19/055503)

## Abstract

We present a passive optical remote sensing technique for recovering shape information about a water surface, in the form of a two-dimensional slope map. The method, known as polarimetric slope sensing (PSS), uses the relationship between surface orientation and the change in polarization of reflected light to infer the instantaneous two-dimensional slope across the field-of-view of an imaging polarimeter. For unpolarized skylight, the polarization orientation and degree of linear polarization of the reflected skylight provide sufficient information to determine the local surface slope vectors. A controlled laboratory experiment was carried out in a wave tank with mechanically generated gravity waves. A second study was performed from a pier on the Hudson River, near Lamont-Doherty Earth Observatory. We demonstrated that the two-dimensional slope field of short gravity waves could be recovered accurately without interfering with the fluid dynamics of the air or water, and water surface features appear remarkably realistic. The combined field and laboratory results demonstrate that the polarimetric camera gives a robust characterization of the fine-scale surface wave features that are intrinsic to wind-driven air–sea interaction processes.

**Keywords:** polarimetric imaging, sea surface roughness, wind waves, ocean wave slope, sea surface slope, capillary waves, gravity waves, wave breaking

 This article features online multimedia enhancements

(Some figures in this article are in colour only in the electronic version)

## 1. Introduction

### 1.1. Overview of short wave measurements

Short ocean waves are primary contributors to the roughness of the wind-driven sea surface, and are of fundamental geophysical and technological importance. Detailed knowledge of the length and timescales of the waves constituting this roughness is crucial to accurate interpretation of oceanic and marine meteorological properties obtained from a number of microwave remote sensing techniques, for quantifying optical transmission and scattering through the

sea surface, and to the understanding of air–sea interaction processes that control the growth and decay of wind waves, transfer energy, govern gas exchange and drive ocean circulation. In the ocean environment, special techniques are needed to measure these short waves, as they can be easily disturbed by the measuring instruments and their mounting structures. Further, the fact that the short waves are usually riding on large-scale dominant sea waves adds significantly to the measurement challenge.

The desired characterization of the short waves is arguably spacetime maps of the sea surface topography, measured over spatial areas of a few square meters and resolved to

millimeter wavelengths. The temporal sampling rate needs to be sufficiently high to allow for Doppler shifting by the orbital velocities of long waves, which can exceed the intrinsic phase speed of the short waves. This goal has been unattainable with available wave measurement technologies. We now briefly review the capabilities and shortcomings of existing techniques.

*1.1.1. Wave wire gauges.* Wave wire impedance probes have been used extensively in laboratory wave height measurements and also in field investigations from both fixed and floating open ocean platforms (Leykin and Rosenberg 1984). They provide a reliable point measurement of the temporal variation of the surface elevation. However, they are vulnerable to mechanical damage, electrical interference and electrochemical problems, and require sufficient dynamic range to embrace the dominant wave height while resolving the short-scale roughness riding on underlying longer waves. Deploying shorter wave wire gauges from floating buoys minimizes certain of these shortcomings, but eliminating spurious short waves that interfere with the measurement is not trivial. Arranging a number of these wire gauges in a spatial array captures spatial and directional information about the waves.

*1.1.2. Optical techniques.* Devices relying on optical probing of the waves have grown in popularity since the advent of lasers and digital imaging systems. One such technique images the length of a subsurface vertically incident laser beam, usually on the water side, from which the wave height at a fixed location can be monitored (Liu and Lin 1982). This technique has been extended to imaging a thin vertical light sheet on the water side to give spatio-temporal wave information along the plane of the sheet (Duncan *et al* 1994a, 1994b, 1999). Both of these techniques have been exploited in laboratory studies. Other laser-based methods include nadir-looking laser altimeters that rely on time-of-flight of pulse reflections. Here, spot size and timing accuracy control the minimum resolved scales. Typical height and wavelength resolution are better than  $\pm 2$  cm and 10 cm, respectively, from a height of 10 m above mean sea level and will depend on the laser beam divergence (in this case 2.8 mrad, Riegl Inc.; see, e.g., Sun *et al* (2005)).

Since the amplitudes of short waves typically scale as  $O(0.1)$  of the wavelength, their slope properties become the preferred mode of detection to resolve the shortest components of the sea surface microstructure, i.e. wavelets approaching capillary scales. The refraction of a single fixed laser beam incident normally from above to an air–water interface provides a time series of the slope vector at a given point (e.g. Jähne and Schultz (1992)). Scanning the horizontal position of the incident beam sufficiently rapidly can provide a spatial map of the resolved wave field (Bock and Hara 1995). Such refractive techniques at a single point (Jähne *et al* 1987) and scanning slope systems (Bock *et al* 1999, Hwang *et al* 1996, 2000) are well suited to measuring short waves and have been used successfully in laboratory and field studies of air–sea interaction and gas exchange studies. Field campaigns

that uniquely capture the surface roughness characteristics are limited to short wave scales due to the difficulty in adequately following/tracking the larger-scale ocean waves.

The refraction of light rays has also been exploited to provide slope field maps of short wind waves using a graduated light target, almost exclusively in laboratory studies (Jähne and Riemer 1990, Keller and Gotwols 1983). Typically, a subsurface light box is set up to display a linearly tapered intensity of a given color along a given direction, with a similar arrangement using a different color taper orthogonal to that direction. This is readily achieved using a plasma or LCD screen display programmed from a PC. Nadir look video image sequences of the distorted light field can be processed to generate vector slope maps describing the spacetime evolution of the resolved wave scales. This technique is well suited to laboratory studies where the subsurface light box can be sited below the tank floor. For field studies, the subsurface package containing the tapered color image target potentially influences the subsurface flow field and is subject to hydrodynamic loading from the large-scale wave orbital motion, which has limited use in the field (Klinke and Jähne 1995).

*1.1.3. Remotely sensed optical roughness techniques.* The use of passive imagery was investigated by Stillwell and Pilon (1974), who proposed that under diffuse sky illumination, the grayscale variation field in a photographic image of the sea surface mirrors the wave slope field. Such lighting conditions are relatively restrictive, and sun glint compromises the results. Validating the technique was not straightforward and it failed to generate a significant scientific following. On the other hand, sun glint provides a robust measure of the mean-squared slope of the sea surface roughness integrated over all scales. Measurements of sun glint were exploited by Cox and Munk (1954a, 1954b), who quantified how the mean-squared sea surface slope varied with wind speed. Their results remain the trusted benchmark. However, this integrated measure of sea surface roughness provides little information on the steepness or energy distribution with respect to scale.

With the aim of resolving wave energy with respect to the length scale and direction, stereophotogrammetry has been used to obtain spatial maps of the sea surface elevation at different times. The classical ‘shape-from-shading’ approach requires optical image roughness subscale to the scale to be resolved, which effectively precludes measuring capillary scale waves (see Jähne *et al* (1992, 1994)). Noise in the inferred wave heights effectively limits the technique to resolving heights of waves of  $O(20$  cm) wavelength and requires diffuse sky lighting (cloud covered conditions). The presence of sun glint degrades this technique. A novel stereophotogrammetric technique proposed by Schultz (1994, 1996) relies on light imaged through specular point backscatter and is therefore sensitive to wave slope rather than wave height, and hence intrinsically better suited for resolving sea surface microstructure. This technique, known as specular surface stereo, determines the two-dimensional slope field of the ocean surface and requires the precise alignment of three spatially separated cameras plus a laser slope gauge for determining the location of a few seed points. In addition, computational

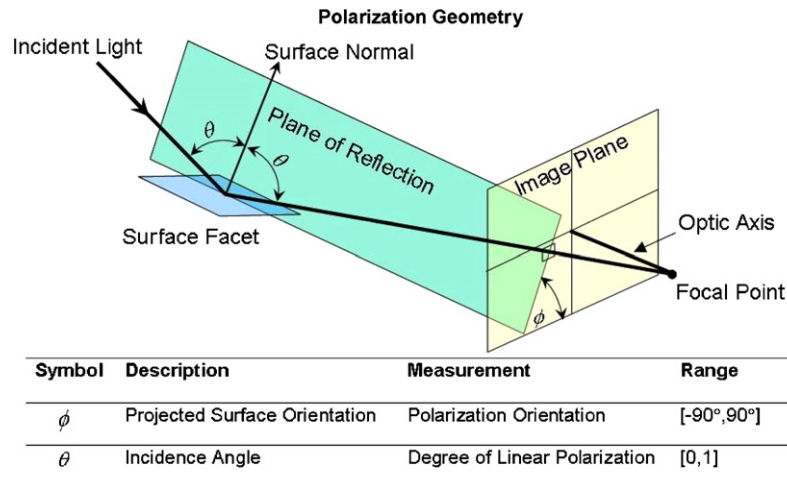


**Figure 1.** The geometric relationship between the surface normal, incidence angle relative to the surface facet ( $\theta$ ) and polarization orientation ( $\phi$ ).

requirements on the retrieval process are complex requiring a global optimization technique to recover the two-dimensional slope field.

The major shortcomings for field applications of the various light sensing methods described above have been to extract sufficient information to infer the full two-dimensional slope field and to construct an instrument that does not disturb the air–sea interface. This overview provides the technical context for the present investigation of polarimetric imaging. It is shown below that this approach overcomes most, if not all, of the shortcomings of each of the foregoing techniques and provides an accurate, remotely sensed measurement of time-varying short wave slope fields at video framing rates. Remote sensing<sup>6</sup> offers the greatest promise for solving these measurement problems.

1.2. Polarimetric slope sensing technique

Conventional optical remote sensing techniques rely only on light amplitude and frequency to provide information about the scattering surface. In this study, we conducted a proof-of-concept study to assess the effectiveness of a passive optical technique based on measuring the polarization properties of light to provide information about the scattering medium.

The polarimetric slope sensing (PSS) concept exploits the polarimetric properties of light scattered from the air–water boundary to recover the instantaneous two-dimensional slope field of a water surface. The wave slope  $\nabla\eta(x, t)$  is the gradient of the water surface elevation  $\eta(x, t)$ . The PSS concept is based upon recovering local surface orientation from specularly reflected light (Wolff 1987, Wolff and Boulton 1991). In the case of a smooth water surface, this can be described in terms of the geometry shown in figure 1. The incident light ray strikes the smooth surface facet and

reflects toward the image plane (e.g., the CCD image sensor). The fundamental optical rule of reflection (derived from the conservation of electromagnetic energy) states that the incidence angle equals the reflection angle, and that the incident ray, the surface normal and the reflected ray lie on a plane (the plane of reflection) that is perpendicular to the surface facet. Polarization of the incident and reflected light rays are specified in the coordinate system defined by the surface normal, the plane of reflection and the surface facet. The polarization orientation,  $\Phi$ , is  $90^\circ$  from the angle  $\phi$  formed by the intersection of the plane of reflection with the image plane (Wolff and Boulton 1991). The incidence angle,  $\theta$ , is the angle the incident ray makes with the surface normal. Together ( $\theta, \phi$ ) define the orientation of the surface normal relative to the camera coordinate system. The origin of the camera coordinate system is the focal point, the z-axis is the optic axis and the x–y plane is parallel to the image sensor. A coordinate transformation between the camera and fixed world coordinate systems is needed to calculate the orientation of the surface normal relative to the Earth. The camera-to-world transformation requires geometric calibration information, which may come in the form of ground control points (objects visible in the scene with known world coordinates), survey data (measurements of the camera position and attitude) or geometric constraints. When a water surface is observed, it is usually possible to impose a flatness constraint that the long-term average slope of the water surface must be zero.

Our goal is to recover the two-dimensional slope field of a water surface by carefully measuring the polarimetric properties of light reflected from and transmitted through the surface. The polarization state of a bundle of incoherent light rays is fully specified by the Stokes parameters, which were first described by Stokes (1852). The Stokes vector  $\mathbf{S} = (S_0, S_1, S_2, S_3)$ , where  $S_0$  defines the intensity of light,  $S_1$  and  $S_2$  define the degree of linear polarization and  $S_3$  defines the degree of circular polarization. Kattawar and Adams (1989) used Mueller calculus to describe the polarization properties of light reflecting from and refracting through a water surface.

<sup>6</sup> In this paper, we define remote sensing as the process of inferring properties about an object by measuring electromagnetic (EM) radiation scattered from the surface. Passive remote sensing covers cases where the source radiation is independent of the receiver. Remote sensing, as implemented in this paper, does not necessarily require a sensor to be mounted on a satellite.

Mueller calculus treats the Stokes parameters as a vector and states that the effect of an optical element can be modeled by  $S_{out} = \mathbf{M} S_{in}$ , where  $\mathbf{M}$  is the  $4 \times 4$  Mueller matrix. The Mueller matrix contains the optical properties of the air-sea interface and describes how the Stokes parameters change when light interacts with varying media. We build on this work to develop an algorithm for recovering the water surface topography in the form of a two-dimensional slope field from observations of reflected and upwelling skylight. The Stokes vectors for reflected light (air-to-medium)  $S_{AM}$  and transmitted light (medium-to-air)  $S_{MA}$  are given by

$$S_{AM} = R_{AM} S_{SKY} \quad \text{and} \quad S_{MA} = T_{MA} S_{UP}, \quad (1)$$

where  $S_{SKY}$  and  $S_{UP}$  are the Stokes vectors for the bundle of light rays coming from the sky and upwelling from beneath the surface, and  $R_{AM}$  and  $T_{MA}$  are the Mueller matrices for reflection and transmission, respectively (Kattawar and Adams 1989). The explicit forms of the Mueller matrices are

$$R_{AM} = \begin{bmatrix} \alpha + \eta & \alpha - \eta & 0 & 0 \\ \alpha - \eta & \alpha + \eta & 0 & 0 \\ 0 & 0 & \gamma_{Re} & 0 \\ 0 & 0 & 0 & \gamma_{Re} \end{bmatrix}$$

and

$$T_{MA} = \begin{bmatrix} \alpha' + \eta' & \alpha' - \eta' & 0 & 0 \\ \alpha' - \eta' & \alpha' + \eta' & 0 & 0 \\ 0 & 0 & \gamma'_{Re} & 0 \\ 0 & 0 & 0 & \gamma'_{Re} \end{bmatrix}, \quad (2)$$

where

$$\begin{aligned} \alpha &= \frac{1}{2} \left[ \frac{\tan(\theta_i - \theta_t)}{\tan(\theta_i + \theta_t)} \right]^2, & \eta &= \frac{1}{2} \left[ \frac{\sin(\theta_i - \theta_t)}{\sin(\theta_i + \theta_t)} \right]^2, \\ \gamma_{Re} &= \frac{\tan(\theta_i - \theta_t) \sin(\theta_i - \theta_t)}{\tan(\theta_i + \theta_t) \sin(\theta_i + \theta_t)}, \\ \alpha' &= \frac{1}{2} \left[ \frac{2 \sin \theta'_i \sin \theta'_t}{\sin(\theta_i + \theta_t) \cos(\theta_i - \theta_t)} \right]^2, \\ \eta' &= \frac{1}{2} \left[ \frac{2 \sin \theta'_i \sin \theta'_t}{\sin(\theta'_i + \theta'_t)} \right]^2, \\ \gamma'_{Re} &= \frac{4 \sin^2 \theta'_i \sin^2 \theta'_t}{\sin^2(\theta'_i + \theta'_t) \cos(\theta'_i - \theta'_t)}, \end{aligned} \quad (3)$$

and where  $(\alpha, \alpha', \eta, \eta', \gamma, \gamma')$  are the Fresnel reflection coefficients,  $\theta_i$  and  $\theta_t$  are, respectively, the incidence and transmission angles, which are related by Snell's law  $\theta_i = n \cdot \sin(\theta_t)$  through the index of refraction  $n$ . The primes indicate transmission from medium-to-air, in which case the angles of incidence and transmission are reversed,  $\theta'_i = \theta_t$  and  $\theta'_t = \theta_i$ , and the index of refraction is inverted,  $n' = 1/n$ .

The radiance within the field-of-view of the imaging polarimeter can be expressed as an equation relating the observed radiance  $S$  to the sum of reflected sky radiance  $S_{AM}$  and upwelling radiance  $S_{MA}$ :

$$S = S_{AM} + S_{MA} = R_{AM} S_{SKY} + T_{MA} S_{UP}. \quad (4)$$

The Mueller matrices  $R_{AM}$  and  $T_{MA}$  (given in equations (2) and (3)) are implicit functions of the surface slope field. By

carefully measuring or inferring the Stokes vectors  $S, S_{SKY}$  and  $S_{UP}$ , it is possible to reconstruct the surface topography.

A full evaluation of equation (4), however, is beyond the scope of this paper. Instead we demonstrate the feasibility of the PSS technique by choosing laboratory and field conditions that simplify the evaluation of equation (4). In future studies, these restrictions can be loosened up and the range of operational conditions expanded. The observation equation can be simplified dramatically by collecting data when the source radiance  $S_{SKY}$  and  $S_{UP}$  are unpolarized. In the laboratory this condition is achieved by using incandescent lights, and in the field by collecting field data on a heavily overcast day (Waterman 1981). If we further assume that upwelling is negligible, the observation equation can be expressed as

$$S = R_{AM} S_{SKY}, \quad (5)$$

where  $S_{SKY} = I_0 (1, 0, 0, 0)$ . Under these conditions and using the functions expressed in equations (2) and (3), the degree of linear polarization, defined by

$$\text{DOLP}(\theta, n) = \sqrt{\frac{S_1^2 + S_2^2}{S_0^2}}, \quad (6)$$

can be written as

$$\text{DOLP}(\theta, n) = \frac{\alpha(\theta, n) - \eta(\theta, n)}{\alpha(\theta, n) + \eta(\theta, n)}. \quad (7)$$

Since the index of refraction,  $n$ , is known, equation (7) gives a functional relationship between the observable quantity DOLP and the incidence angle  $\theta$ . Note that the sky radiance does not enter into this equation.

When upwelling cannot be neglected, the expression for DOLP becomes

$$\begin{aligned} \text{DOLP}(\theta, n) &= \frac{\alpha(\theta, n) - \eta(\theta, n) + u(\theta, \theta') \cdot (\alpha'(\theta', n') - \eta'(\theta', n'))}{\alpha(\theta, n) + \eta(\theta, n) + u(\theta, \theta') \cdot (\alpha'(\theta', n') + \eta'(\theta', n'))}, \end{aligned} \quad (8)$$

where  $u(\theta, \theta') = S_0^T(\theta') / S_0^R(\theta)$  is the ratio of the transmitted (upwelling) to the reflected radiance. It is important to note that the inclusion of  $u(\theta, \theta')$  in equation (8) adds a dependency of DOLP to the upwelling and sky radiance and that as  $u \rightarrow 0$  equation (8) reverts to the much simpler form of equation (7). The incidence angle calculations are sensitive to upwelling. The polarization orientation of upwelling is parallel to the plane of reflection, and therefore perpendicular to the polarization orientation of reflected light. Because the superposition of these two components is incoherent, and the reflected component is greater than the upwelling component, the polarization orientation remains that of the reflected component. The polarization orientation  $\Phi$  is not affected by upwelling and is given by

$$\Phi = \frac{1}{2} \tan^{-1} \left( \frac{S_2}{S_1} \right). \quad (9)$$

Note that  $\phi = \Phi + 90^\circ$ .

Evaluation of equation (8) requires knowledge of the source radiance (both downwelling sky and upwelling subsurface), which is a complicated function of angle of

incidence. Our goal can be restated as constructing an algorithm that infers the two-dimensional slope field of the surface without any direct measurement of sky or upwelling radiance. We are able to estimate the affects of upwelling by imposing a flatness constraint on the recovered surface. Since the temporal and spatial average of water surface must be zero, we are able to impose an additional constraint on the computed surface normal vectors. First, the algorithm finds the time-varying surface normal vector field by inverting equations (7) and (9) for  $n = 1.33$ . Next, the time-average of the surface normal vectors are computed and subtracted from the time-varying field. The implicit assumption here is that the effects of upwelling (which does not vary with time) can be isolated as a bias two-dimensional slope field. The accuracy of this algorithm depends on the magnitude of  $u(\theta, \theta')$  and the nonlinear transformation used to invert equation (8). We will show the feasibility of this type of upwelling compensation algorithm in sections 3 and 4 where the results are compared with *in situ* observations of surface slope statistics.

### 1.3. Feasibility study

The objective of this study was to test the validity of the PSS concept using a polarimetric imaging system (Equinox Corp.) to measure small-scale sea surface roughness wave characteristics. This would underpin a remote sensing method using a field-deployable polarimetric imaging system for recovering the two-dimensional time-varying slope field of very short wind waves at video frame rates. This paper describes a two-component feasibility study—a laboratory wave tank experiment and a field experiment conducted from the Piermont Pier on the Hudson River in New York, USA. The extracted field of surface normals from the polarimetric camera system was compared with the surface slope statistics measured by *in situ* techniques.

## 2. Methodology

### 2.1. Equinox polarization camera

The Equinox polarization camera is a 3-channel sensor that uses a proprietary optical beamsplitter design, similar to a 3-chip RGB color camera. The beamsplitter can be configured to measure any combination of three of the four Stokes vector components. The Stokes vector  $\mathbf{S} = (S_0, S_1, S_2, S_3)$ , where

$$\begin{pmatrix} S_0 \\ S_1 \\ S_2 \\ S_3 \end{pmatrix} \equiv \begin{pmatrix} I_0 + I_{90} \\ I_0 - I_{90} \\ I_{45} - I_{135} \\ I_{RC} - I_{LC} \end{pmatrix} \quad (10)$$

with  $I_x$  representing the intensity transmitted through a linear polarizer and retarder in series producing linear polarization at angles  $x = 0^\circ, 45^\circ, 90^\circ, 135^\circ$ , and right and left circular polarizations  $x = RC, LC$ , respectively. In this investigation, the Equinox polarization camera was configured to simultaneously measure  $0^\circ, 45^\circ$  and  $90^\circ$  polarization orientations sufficient to determine a complete state of partial linear polarization (i.e., orientation of polarization and DOLP).

It can be shown (Collett 1993) that the first three Stokes parameters are determined by

$$\begin{pmatrix} S_0 \\ S_1 \\ S_2 \end{pmatrix} \equiv \begin{pmatrix} I_0 + I_{90} \\ I_0 - I_{90} \\ 2I_{45} - (I_0 + I_{90}) \end{pmatrix}, \quad (11)$$

where the circular component of the Stokes vector  $S_3$  is assumed to be insignificant (Liu and Voss 1997, Voss and Liu 1997) and was not measured. Some other design features of the camera are co-registration of the  $I_0, I_{45}$  and  $I_{90}$  images within 1/10 pixel, CCD size of  $1024 \times 1024$  pixels, 12-bit digitization depth, 15 Hz frame rate and an integration time of 20–30 ms.

The Equinox polarization camera was calibrated by measuring the Mueller matrices for each of the three polarization output channels using ellipsometry calibration techniques (Azzam and Bashara 1987). This provided a relationship between incident light with a known polarization and the response of the three calculated polarization camera intensities,  $I_0, I_{45}$  and  $I_{90}$ . The Stokes vector, DOLP and polarization orientation are calculated from equations (11), (7) and (9), respectively.

The accuracy of the Equinox polarimetric camera was determined in Wolff and Boulton (1991) by light reflected from a dielectric plate with a known index of refraction. The smooth blackglass dielectric plate with index of refraction  $n = 1.51$  was mounted on a precision two degrees of freedom rotation stage and viewed by the Equinox camera over a wide range of known azimuth and incidence angles on a laboratory optical bench. Using the known relationship in equation (7), the incidence angle is defined precisely for the known index of refraction and DOLP. The technique used in Wolff and Boulton (1991) for finding surface normals from polarization determined the orientation of solid flat surfaces with good measurement accuracy. The standard deviation of the error in determining the surface normal orientation was consistently calculated to be within  $1^\circ$ .

In the current study, we viewed a smooth water surface in the laboratory and found that the standard deviation of the instantaneous slope value about the smooth surface was  $0.684^\circ$  or 0.012 radians. Furthermore, we observed a slight increase in standard deviation with increasing incidence angle from a nominal value of 0.009 radians below  $40^\circ$  incidence to 0.016 at  $48^\circ$  incidence. The measured values for the smooth water constraint intrinsically define the precision for these experiments.

The direction of the surface normal is found for the water surface facet in the field-of-view of each pixel. The spatial resolution per pixel is  $\sim 0.1$  mm for the laboratory and  $\sim 1$  mm for the field experiments. For the laboratory and field experiments, the placement of the camera was chosen so that the incidence angle did not exceed the Brewster angle ensuring an unambiguous relationship between DOLP and  $\theta$  (the Brewster angle for  $n = 1.33$  is about  $52^\circ$ ). The maximum anticipated wave slope was less than  $8^\circ$  and the camera incidence angle was  $40^\circ$  in the laboratory and  $60^\circ$  in the field. For isolated instances when there is an ambiguous relationship, such as in breaking waves, the processing

algorithm determines the slope on the approach side of the Brewster angle. The observable surface slope is limited by the inclination of the camera such that the incident ray must come from the sky. For example, if the camera has an incidence angle of  $45^\circ$ , the surface slope can have a maximum of  $67.5^\circ$  toward the camera and  $22.5^\circ$  away from the camera. Each time the inclination angle of the camera is changed, the range of possible slopes needs to be determined.

The PSS technique implemented in this investigation assumes that incident illumination is unpolarized. This is closely approximated by lighting conditions during an overcast sky. A more detailed methodology beyond the scope of this investigation needs to be implemented for sunny and partly cloudy weather conditions where illumination of skylight is partially linearly polarized dependent upon the region of the sky and the position of the sun. Fortunately, under all such sky weather conditions, polarization-based recovery of water surface orientation only requires the measurement of the first three of the four Stokes parameters. Waterman (1981) observed that at least 99% of naturally occurring light consists of some form of partial linear polarization having no circularly polarized component. Since skylight is predominantly linearly polarized, the circular polarization component of the Stokes vector may be neglected for certain sky conditions and viewing geometries.

## 2.2. Laboratory experiment

A controlled laboratory tank experiment was carried out with mechanically generated gravity waves at Lamont-Doherty Earth Observatory. The aim was to provide controlled conditions for testing the polarimetric slope sensing concept. The tank was  $1\text{ m} \times 1\text{ m} \times 0.3\text{ m}$  (deep), lined with black neoprene to minimize the light transmitted from below the air–water interface, and filled with tap water. The waves were generated using a vertically oscillating cylindrical wave maker. A capacitance wire wave gauge with a 200 mm element sampled the surface displacement at 100 Hz with a resolution better than 0.1 mm and a linearity of better than  $\pm 1\%$  of its 200 mm range. This probe has excellent long-term stability as demonstrated by approximately monthly static calibrations. The mechanical waves were generated with a dominant frequency close to 5 Hz and a phase speed of about  $0.3\text{ m s}^{-1}$ . This choice of wave speed minimized blurring due to the 20 ms integration time of the polarimetric camera. The wave gauge provides an independent measurement estimate of slope,  $1/C \times \partial\eta/\partial t$ , assuming the waves are linear, where  $C$  is the phase speed of the dominant wave,  $\eta$  is the surface displacement and  $t$  is the time. On the side of the tank opposite the wave maker, synthetic horsehair was placed to absorb the wave energy and minimize wave reflection. An array of high-intensity incandescent floor-standing lamps diffusely reflecting from matte white wall and ceiling liners provided ambient lighting that closely approximated unpolarized incident illumination. The robustness of the technique was investigated by varying the paddle oscillation amplitude using two stroke conditions and varying the azimuthal viewing orientation of the polarimetric camera for

**Table 1.** Polarimetric camera measurements from the laboratory study.

Case	Camera look direction	Wave paddle stroke
1	Perpendicular to wave propagation	Small
2	Perpendicular to wave propagation	Large
3	Oblique to wave propagation ( $45^\circ$ )	Large
4	Oblique to wave propagation ( $45^\circ$ )	Small
5	Parallel to wave propagation	Small
6	Parallel to wave propagation	Large
7	Parallel to wave propagation	Wind-generated waves

three look directions (parallel, at  $45^\circ$  and perpendicular to the wave propagation direction). The steepness of the wave field was observed to be within 5–10% across the tank at a given distance from the wave maker and to decay linearly with distance from the wave maker by 43% over the working section of the tank for both wave paddle strokes. The experimental configuration (including multiple incandescent lamps and the wave-maker mechanism) constrained the bore-sighted polarimetric camera locations in the working section of the tank to different distances from the wave maker and across the tank for the three viewing azimuths. This required correcting the *in situ* wave slopes at the bore-sighted locations of the polarimetric camera. This was carried out in the data processing using the slopes measured by the wave probe at a fixed location and the known wave slope variability in the tank. The vertical orientation of the polarization camera mounted on a tripod was measured to be  $40^\circ$  from nadir with a plumb bob and a protractor. The tripod was moved into different positions to achieve the three different azimuth orientations. We also conducted a trial with short wind-generated waves, to investigate the effects of capillary waves and slope discontinuities associated with microscale breakers. A summary of these cases is given in table 1.

## 2.3. Field experiment

The second phase of this study was performed from the Piermont Pier on the Hudson River, near Lamont-Doherty Earth Observatory, on 30 August 2006. For the field experiment, we used a Riegl model LD90-3100VHS laser rangefinder to measure the wave heights within the field-of-view of the polarimetric imager. The laser altimeter was boomed out over the water surface at a height of 1.5 m and sampled at 20 Hz with a distance resolution of 1 cm and a 2.8 mrad beam divergence (1 mrad corresponds to 10 cm beam width per 100 m of distance). The laser altimeter provides an independent measurement of the slope,  $1/C \times \partial\eta/\partial t$ , in a manner similar to the wave wire probe used in the laboratory experiment. The polarimetric camera viewed the water surface directly beneath the laser altimeter with a vertical viewing orientation of roughly  $60^\circ$  from nadir. Here, the camera was deployed in a fixed configuration from run to run throughout the field experiments on the Piermont Pier. The look angle was oblique, at roughly  $45^\circ$  to the oncoming wave field, at a fixed azimuth angle relative to the pier. A day was chosen when the sky conditions were mostly overcast, which

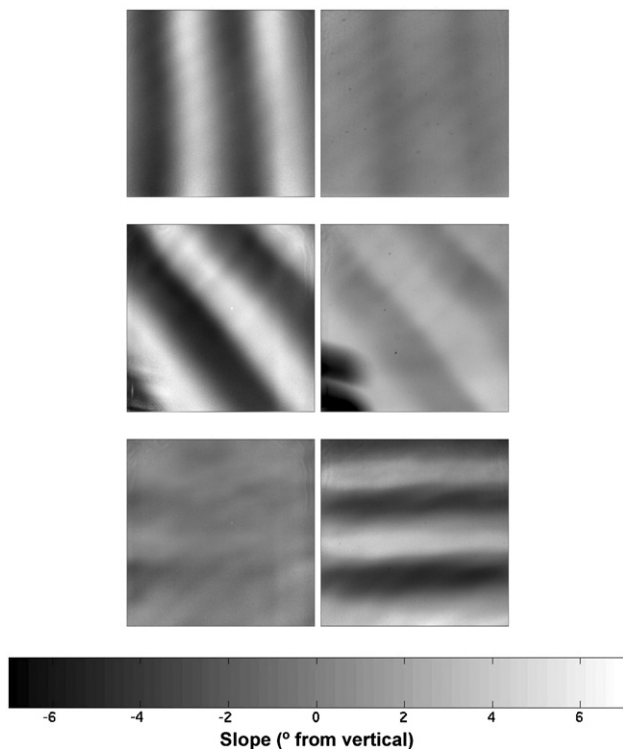


**Figure 2.** Polarimetric image frame pairs from three laboratory experimental runs showing the slope of the water surface. For each pair, the image on the left is the  $x$ -direction (cross-look-direction) slope and the image on the right is the  $y$ -direction (look-direction) slope. The top pair is for the camera look direction perpendicular to the wave propagation direction. The middle pair from the top is for the camera look direction  $45^\circ$  to the wave propagation direction. The bottom pair from the top is for the camera look direction into the wave propagation direction. Note that the distortion in the lower left corner of the  $45^\circ$  case is due to a polarized reflection that affects the slope. This region is not considered in subsequent analysis. The field-of-view in all images is roughly  $12.9\text{ cm} \times 16.8\text{ cm}$ . Movies of these cases are available as multimedia attachments.

was important for our test of the polarimetric technique. The wind speed that day was moderate at  $3\text{--}5\text{ m s}^{-1}$ , and included short bursts of gustiness. The overcast sky provides a good approximation to the desired natural condition of uniformly unpolarized lighting. This phase of the evaluation allowed us to become more familiar with additional challenges associated with natural lighting—sky radiance polarization variations, upwelling radiance and sun glint, amongst others. Staging the field phase in overcast conditions minimized these effects.

### 3. Results

A technical evaluation of the polarization camera requires a comparison of the surface wave field as determined by the polarimetric image data with that from a robust *in situ* wave gauge. Monochromatic waves generated in the laboratory tank had root-mean-square (rms) slopes between 0.04 and 0.12. The former was chosen to be in the linear range and was validated for sinusoidal shape and linear dispersion, and the

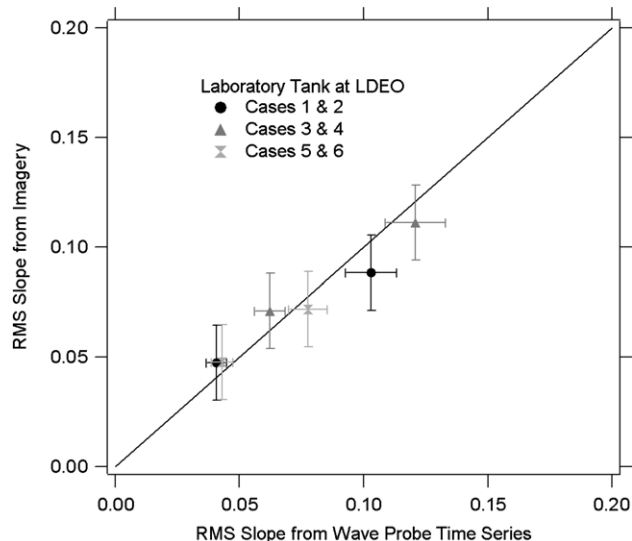


**Figure 3.** Total rms wave slope from the polarimetric imagery versus the total rms wave slope determined from the *in situ* wave probe. Uncertainty bounds show the variability in the polarimetric camera calibration and the wave slope variability in the tank at the known image locations. Cases 1 and 2 are for the camera look direction perpendicular to the wave propagation direction, cases 3 and 4 are for the camera look direction  $45^\circ$  to the wave propagation direction and cases 5 and 6 are for the camera look direction into the wave propagation direction.

latter were in the weakly nonlinear regime. The lowest-order nonlinear correction to the linear phase speed of the dominant wave was applied to the wave gauge data. This is given by  $C_{nl}^2 = C_1^2(1 + a^2k^2)$ , where  $C_{nl}$  is the phase speed of the dominant nonlinear wave,  $C_1$  is the linear phase speed,  $a$  is the amplitude and  $k$  is the wavenumber (Lamb 1945).

Figure 2 shows the slope imagery from the linear wave slope cases 1, 4 and 5. For cases 1–6, the mean wavelength determined from zero-crossings in the slope imagery was  $6.42 \pm 0.66\text{ cm}$  and the dominant wavelength determined in the wave spectrum was  $6.63 \pm 0.53\text{ cm}$ . A direct comparison of the wave slope determined from the polarimetric imagery and *in situ* wire wave gauge is made in figure 3. This figure shows the total rms wave slope from the polarimetric imagery versus the rms wave slope determined from  $1/C \times \partial\eta/\partial t$  described above. The total slope at each pixel in an image is defined by  $\sqrt{S_x^2 + S_y^2}$ , where  $S_x$  and  $S_y$  are the  $x$  and  $y$  components of slope, respectively. The bias slope field was estimated by averaging each pixel over all frames. As described in section 1.2, the bias slope field is attributed to upwelling and errors in measuring the camera’s inclination angle. For the laboratory experiment, however, the bias slope field was less than the measurement precision. The bias slope field was subtracted from each individual slope image. The total rms wave slope was computed using all pixels in all images in that run. For a given incidence angle, the results show a strong correlation to the known wave slope in each azimuth orientation. The coefficient of determination for the results in figure 3 is 0.98. Potential sources for the variability in figure 3 are: the

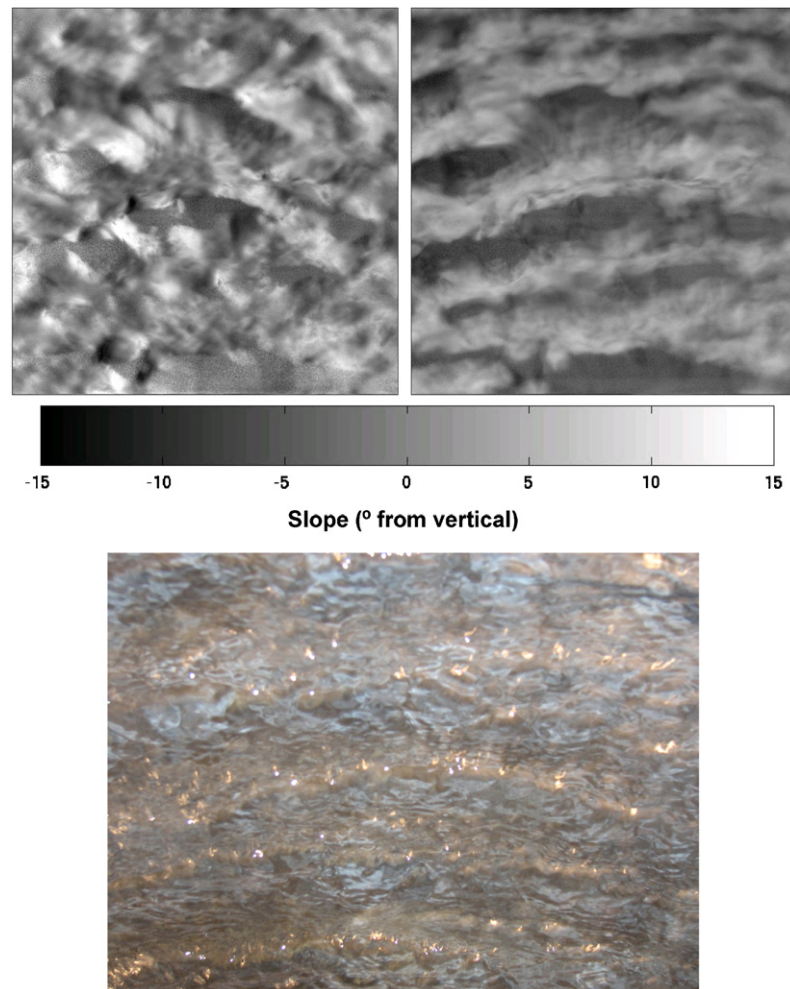


**Figure 4.** Top: polarimetric image frame pairs from the laboratory experimental case showing the slope of a wind-roughened water surface without mechanically generated waves where the camera look direction is into the wind. Some of the fast-moving wind waves are blurred by the 20 ms integration time of the polarimetric camera. The image on the left is the  $x$ -direction (cross-look-direction) slope and the image on the right is the  $y$ -direction (look-direction) slope. The field-of-view in the images is roughly  $12.9 \text{ cm} \times 16.8 \text{ cm}$ . Bottom: photograph of the wind-roughened surface in the Lamont-Doherty Earth Observatory wave tank for the same look direction as in the slope imagery.

polarimetric camera calibration (section 2.1), the variation in distance of the bore-sighted imagery from the wave generator and across the tank (section 2.2) and any non-uniformity in the background incident polarized light. The first two sources have been estimated and their associated uncertainties are shown in figure 3. The non-uniformity of background incident polarized light is not precisely known, but is believed to be minimal based upon surveys with an instrument that can only detect significant polarization gradients. The high correlation in figure 3 demonstrates that the slope results from the polarimetric camera provide a robust characterization of the repeatable short gravity wave system.

Examples of intense wind-forced capillary-gravity waves were also generated in the laboratory tank. Figure 4 shows the along- and cross-look wave slope images for the wind-roughened surface as well as an image of the wave conditions from the same perspective as the polarimetric camera. Some of the fast-moving wind waves are blurred by the 20 ms integration time of the polarimetric camera. Mechanically

generated waves were not present. It is clear that the dominant waves exist in the along-look direction with alternating positively and negatively slope features, while the cross-look slope shows the more random slope features of small-scale turbulent structures evident during wind-wave breaking (Siddiqui *et al* 2004, Zappa *et al* 2004). The measured total rms wave slope from these polarimetric images was  $0.10 \pm 0.01$ . This is comparable to the wind-forced wave conditions measured at short fetch in linear wind-wave tanks (Jähne *et al* 1987) and at unlimited fetch in annular wind-wave tanks (Bock *et al* 1999, Jähne *et al* 1987).

Following the success of the laboratory phase in delivering robust, reliable slope field data, we performed a field experiment at the Piermont Pier described in section 2.3. Slope imagery ( $x$  and  $y$  components) from the field is shown in figure 5. The top pair is the raw image slope as determined from the polarimetric camera. The slope arrays produced from the field experiments showed a bias in the form of a nonzero temporally averaged slope. The bias slope field was estimated

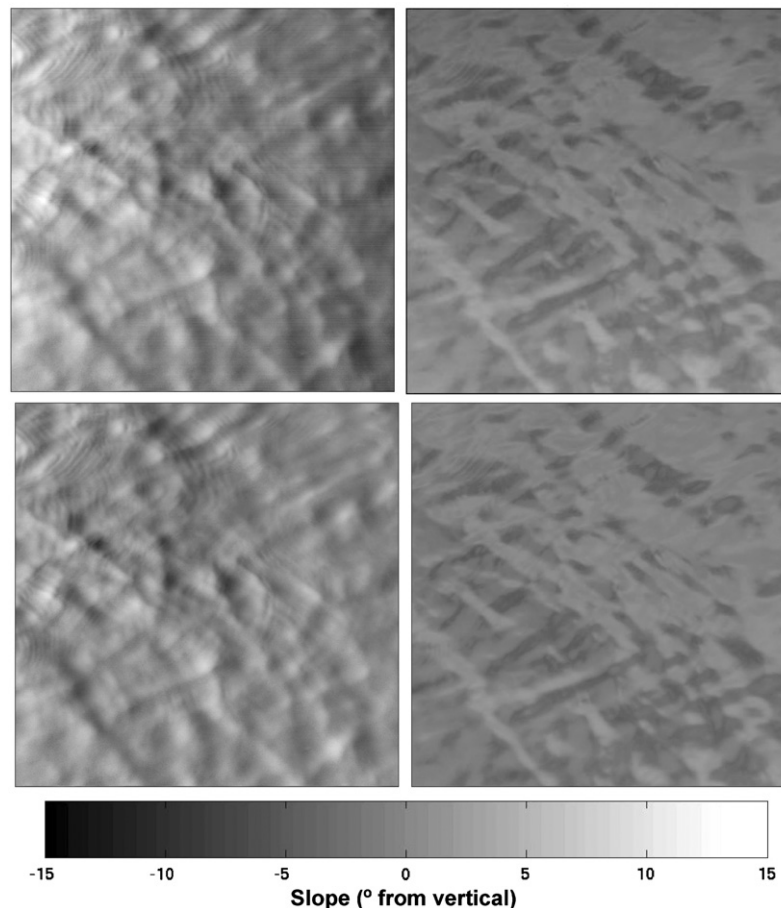


**Figure 5.** Polarimetric image frame pairs from run 4 of the Piermont Pier experiment showing the slope of the water surface. For each pair, the image on the left is the  $x$ -direction (cross-look-direction) slope and the image on the right is the  $y$ -direction (look-direction) slope. The top pair is the raw image slope as determined from the polarimetric camera. The bottom pair has the image bias removed using a temporal reconstruction. The field-of-view in all images is roughly  $1.3 \text{ m} \times 2.6 \text{ m}$ . A movie of this case is available as a multimedia attachment.

by averaging each pixel over all frames. As described in section 1.2, the bias slope field is attributed to upwelling and errors in measuring the camera's inclination angle. For the bottom pair, the bias slope field was subtracted from each individual slope image. The comparison of the two pairs shows the distinct non-uniform bias with a maximum magnitude of approximately  $2^\circ$ . The water surface structure shows short wind waves of  $O(10 \text{ cm})$  wavelength propagating across the image from left to right. The structure of the wind-roughened surface is similar to that observed in figure 4. Another time series of slope imagery ( $x$  and  $y$ ) at the Piermont Pier is shown in figure 6. The image time series shows the passage of one breaking wave in the lower portion of the image and a second wave beginning to break in the upper-left portion. Both breaking waves that propagated through the sequence had a wavelength of  $O(1 \text{ m})$ . In this case, the fine-scale structure of the breaking crest and its trailing wake are captured without blurring by the polarimetric camera. The wind-roughened surface structure seen in figure 5 was not observed and longer gravity waves of  $O(10 \text{ cm} - 1 \text{ m})$  had developed.

A direct comparison of the wave slope on the Hudson River determined from the polarimetric imagery and Riegl

laser altimeter is made in figure 7. This figure shows the total rms wave slope from the polarimetric imagery versus the rms wave slope determined from  $1/C \times \partial\eta/\partial t$  using the laser altimeter. Slope statistics are computed over the image. Note that small boats passing caused waves that propagated into the image field-of-view in addition to the existing surface waves on the Hudson River. The dominant waves were of the same scale as the image size. The frequency of the dominant waves determined from time series of the wave slope imagery and of the Riegl laser altimeter were the same and ranged from 0.45 Hz to 0.72 Hz for the data conditions presented in the field. The coefficient of determination for the results in figure 7 is 0.98 and demonstrates that the slope results from the polarimetric camera provides a robust characterization of the fine-scale surface wave features intrinsic to wind-driven air-sea interaction processes.

In this scenario, the calculated total rms wave slope is a combination of the scale of the larger waves in addition to the smaller scale wave slopes that contribute to the total rms wave slope. The total rms wave slope estimates calculated from the polarimetric images match the slope calculated from the Riegl. The spot size of the Riegl is sufficient to capture most

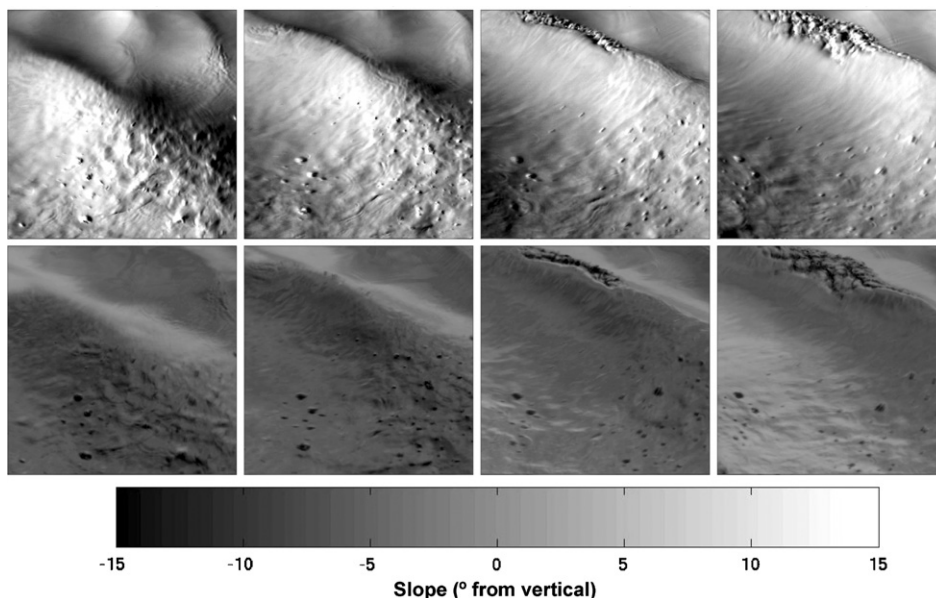


**Figure 6.** Polarimetric image frame time series with the bias removed during the Piermont Pier experiment showing the slope of the water surface at the completion of one breaking wave and as a second wave begins to break. The images on the top are the  $x$ -direction (cross-look-direction) slope and the images on the bottom are the  $y$ -direction (look-direction) slope. The field-of-view in all images is roughly  $1.3 \times 2.6$  m. The images are separated by 0.13 s. A movie of this case is available as a multimedia attachment.

of the wave slope variability at the smallest scales that existed during these experiments since the estimates of slope match perfectly. In addition, the polarimetric imagery in figure 5 shows the small-scale structure that is expected at the smaller scales as observed in the laboratory wind-roughened surface in figure 4. Only when the field-of-view is of a flat-water surface will the average and rms slopes be zero. Since the rms surface slope is an additive quantity, any deviation from a flat-water surface within the field-of-view will contribute to the total rms wave slope. This includes any surface deformation such as those caused by wind or free-surface turbulence that is present in the scene.

The polarimeter in conjunction with the wave wire in the laboratory and the laser altimeter in the field provide statistically independent measures of the aggregate response. While the comparison does not provide a measure of slope for specific pixels, the direct comparison of the rms wave slopes derived from the polarimeter to the wave probes is a measure of the accuracy (figures 3 and 7). Since we know by direct measurement that the accuracy is within our error bounds, we can infer that the effect of all errors (including upwelling) on accuracy is within the error bounds.

#### 4. Discussion

The success of the laboratory and field deployments for validation of the PSS technique opens up many new possibilities to make groundbreaking studies in air–sea interaction processes that are controlled by the sea surface microstructure. Increasing evidence accumulated over the past two decades in laboratory experiments indicates that the air–sea gas transfer, such as for the sparingly soluble

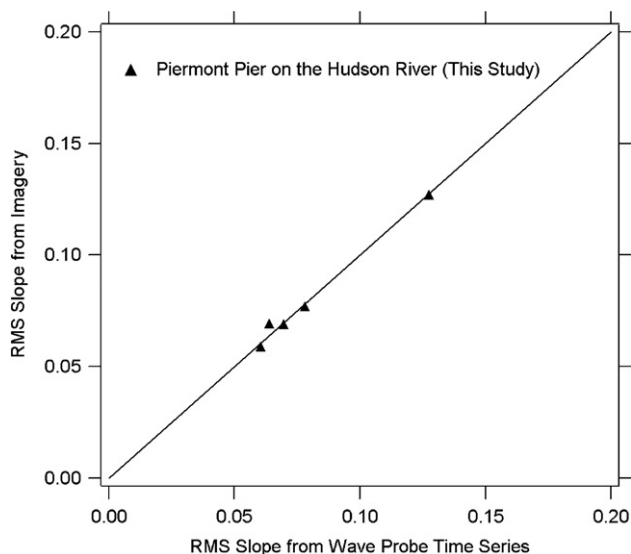


**Figure 7.** Comparison of polarization camera and laser altimeter results. Scatter plot of the total root-mean-square slope from the polarimetric imagery versus the total root-mean-square wave slope from the laser altimeter during the field experiment at the Piermont Pier on the Hudson River.

gas  $\text{CO}_2$ , strongly correlates with water surface roughness or the mean-squared slope of short wind waves (Bock *et al* 1999, Jähne *et al* 1987), and is independent of the presence of surface-active material. In the presence of surface films, gas transfer may be significantly reduced at a given wind speed or wind stress. Surfactants can also significantly damp waves at high wavenumbers and thus affect wave slope spectra, and can suppress near-surface turbulence at low wind speeds

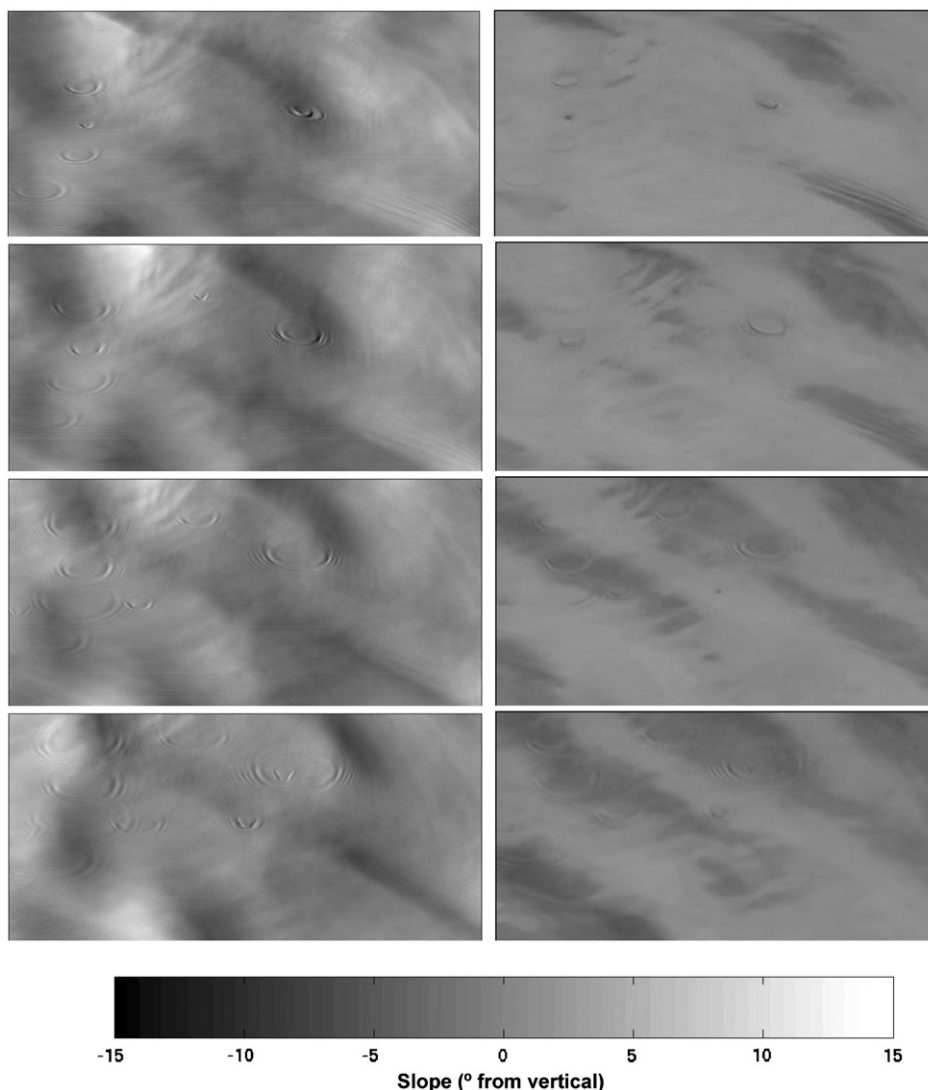


**Figure 8.** A time series example of ring waves captured by the PSS system at the Piermont Pier. The  $x$ -direction slope is on the left and the  $y$ -direction slope is on the right. The field-of-view in all images is roughly  $1.3 \text{ m} \times 1.3 \text{ m}$ . The images are separated by  $0.07 \text{ s}$ .

(Bock *et al* 1999). Microscale wave breaking has been suggested as a dominant mechanism for gas transfer at low to moderate wind speeds over the ocean (Zappa *et al* 2001, 2004) and may explain the observed correlation between gas transfer and surface roughness. The PSS system provides for the first time the capability of characterizing the wind-driven sea surface microstructure down to capillary scales in the field without disturbing the air–sea interface. These measurements are important for understanding the gas transfer processes that are relevant in the field.

The PSS system would also be useful in improving our understanding of radar scattering from the sea surface, especially in precipitating conditions when the small-scale roughness is modified by raindrops impinging on the surface (Yang *et al* 1997). Le Mehaute and Khangaonkar (1990) established the dynamic effect of intense rain on water waves, demonstrating that vertically falling rain dampens wind waves, but rainfall in high winds contributes to the growth of the

amplitude of waves. Satellite-based scatterometer radars are routinely used to estimate sea surface winds (e.g. NASA's SeaWinds on QuikScat and ESA's ASCAT on Envisat) through empirically derived relationships between radar echo intensity and surface wind speed. Rain produces circular *ring waves* on the surface that modify the directional signature of the radar scattering and thereby introducing a source of error. Polarimetric imaging would allow the capture of the dynamics of these interactions. During this study, we found a sequence of polarimetric images that captured a series of ring waves probably caused by bursting bubbles or stray raindrops. Figure 8 shows a time series of the  $x$  and  $y$  components of surface slope. To the best of our knowledge, this is the first time the three-dimensional history of this type of wave motion has been captured. With simultaneous observations using microwave radar, it should be possible to deduce the effect of ring waves on the microwave signature in both laboratory and field conditions.

The effect of surface slicks on waves has also received considerable attention (Bock *et al* 1999, Jähne *et al* 1987, Tang and Wu 1992, Wei and Wu 1992, Zappa *et al* 2004). These studies show that films intensify the damping of the short waves, which in turn reduces the surface roughness and consequently the wind stress. Zappa *et al* (2004) compared refractive slope imaging techniques with *in situ* wave wire measurements. Much of the variability in Zappa *et al* (2004) was due to damping by surface-active material of small-scale waves that are not capable of measurement by *in situ* wave wire probes. With cleaner air–water interfaces, the higher density of capillaries that exists contributes to the total rms slope and is measured by slope imaging techniques while often missed by wave-wire techniques. This is evident in Zappa *et al* (2004) measurements that show the wave wire is routinely biased low compared to the image slope. By including the ability to measure subtle changes in elliptical polarization and the ability to model the effects of organic material near the surface, the PSS system will provide a powerful means for studying the interaction of biological processes on air–sea interaction, the exchange of climatically important trace gases and radar backscatter.

This study has been limited to surfaces that are relatively smooth within the pixel field-of-view. However, a fundamental technical issue in remote sensing is subpixel variability. For polarimetric imaging of surface slope field, this concern is significant since the slope variability is of the same order for both large- and small-scale waves. Steep capillary waves riding on longer gravity waves themselves riding on deep ocean swell provide ample opportunity for influencing the retrieved slope from polarimetric imaging. It is clear that the resolution of the imaging camera is crucial to understanding the desired process since waves of various scale contribute similar magnitudes to the derived slope field. The resolution will define the scale at which the characteristic of the subpixel variability is important. For example, if the horizontal resolution of the camera is of order 10 cm, all short capillary waves will be averaged into the pixel. If the capillaries fill the whole nadir-looking pixel, their mean contribution may effectively be nearly zero for linear waves and no information about the longer swell waves is lost due to the presence of these capillary waves. The capillaries will cause no spurious slope artifacts on the larger-scale waves greater than 10 cm. Spurious artifacts may arise (i) for cases of high incidence angles when shadowing may cause preferential slopes to be averaged into the pixel and (ii) for cases where the capillaries fill only a portion of the pixel.

Further experiments are needed to determine the effect of a polarized sky. This paper examines the special case of unpolarized skylight (which is typical of an overcast sky). We determined using handheld filters that there was no apparent polarization for both the laboratory and sky downwelling. For this case, the surface orientation can be deduced from measurements of the degree of linear polarization and the polarization orientation. In the general case, where skylight is partially linearly polarized (the sky will have an insignificant circular polarization component,  $S_3$ ), the surface orientation is not uniquely determined from

measurements of the polarization state of the reflected light alone, and additional information about the polarization state of the skylight is needed. The polarization distribution of the sky can be measured with a second imaging polarimeter looking up at the sky (Liu and Voss 1997). Equation (5) holds for the polarized case as well, but  $S_0$ ,  $S_1$  and  $S_2$  of  $S_{\text{SKY}}$  will now be nonzero components that have an angular dependence based on the direction of the downwelling ray.

## 5. Conclusion

This feasibility study has validated the polarimetric slope sensing concept. We demonstrated that the two-dimensional slope field of short gravity waves can be accurately recovered from a distance without interfering with the fluid dynamics of the air or water, and the recovered water surface appears remarkably realistic. In the laboratory, the quantitative estimates of slope from the polarimetric camera showed a close correspondence to the *in situ* wave slope measurements. Both the Lamont laboratory and Piermont Pier field results were significantly robust, each with a correlation coefficient of 0.98. The combined field and laboratory results demonstrate that the polarimetric camera gives a robust characterization of the fine-scale surface wave features intrinsic to wind-driven air–sea interaction processes.

The present results provide a strong incentive for developing an advanced imaging polarimeter for measuring the slopes of short waves (including capillaries) in an ocean environment. We were able to draw several conclusions about the instrument requirements for the development of this new camera and for future studies that utilize it. A complete test of the concept under polarized skies would require two polarimetric cameras. One camera measures the incoming sky radiance. The other measures the reflected radiance and upwelled radiance contributions, as we have done here. The camera should have a dynamic range capable of imaging in non-uniformly illuminated sky conditions. The camera should also have an integration time capable of freezing short gravity–capillary waves riding on ocean swell. For example, in the presence of ocean swell, the short gravity–capillary waves travel through the field-of-view with a velocity of up to several meters per second. Thus, to avoid motion blur an integration time of at most 0.1 ms is required. In addition, a 60 Hz frame rate is required to capture the temporal structure of the gravity–capillary waves. Current image sensor and optics technology allows for these shorter integration times and fast frame rates with the necessary sensitivity for oceanographic studies. A follow-on study using the enhanced polarimeter described above in conjunction with an independent slope measurement using, for example, a refractive imaging technique, is needed to verify the PSS technique for capillary waves. Furthermore, to study surface slicks and biological activity in surface waters, it would be desirable for the polarimetric cameras to be able to measure the complete four-component Stokes vector.

## Acknowledgments

This work was funded by the Office of Naval Research under the Radiance Dynamics of the Ocean (RaDyO) DRI grant

number N00014-06-1-0372. We thank Jose L Hernandez for his assistance in processing of the wave slope imagery. This is Lamont-Doherty Earth Observatory contribution number 7153.

## References

- Azzam R M A and Bashara N M 1987 *Ellipsometry and Polarized Light* (Amsterdam: Elsevier)
- Bock E J and Hara T 1995 Optical measurements of capillary-gravity wave spectra using a scanning laser slope gauge *J. Atmos. Oceanic Technol.* **12** 395–403
- Bock E J, Hara T, Frew N M and McGillis W R 1999 Relationship between air-sea gas transfer and short wind waves *J. Geophys. Res.* **104** 25821–31
- Collett E 1993 *Polarized Light: Fundamentals and Applications* (New York: Dekker)
- Cox C and Munk W 1954a Measurement of the roughness of the sea surface from photographs of the sun's glitter *J. Opt. Soc. Am.* **44** 838–50
- Cox C and Munk W 1954b Statistics of the sea surface derived from sun glitter *J. Marine Res.* **13** 198–227
- Duncan J H, Philomin V, Behres M and Kimmel J 1994a The formation of spilling breaking water waves *Phys. Fluids* **6** 2558–60
- Duncan J H, Philomin V, Qiao H and Kimmel J 1994b The formation of a spilling breaker *Phys. Fluids* **6** S2
- Duncan J H, Qiao H, Philomin V and Wenz A 1999 Gentle spilling breakers: crest profile evolution *J. Fluid Mech.* **379** 191–222
- Hwang P A, Atakturk S, Sletten M A and Trizna D B 1996 A study of the wavenumber spectrum of short waves in the ocean *J. Phys. Oceanogr.* **26** 1266–85
- Hwang P A, Krabill W B, Wright C W, Swift R N and Walsh E J 2000 Airborne scanning lidar measurement of ocean waves *Remote Sensing Environ.* **73** 236–46
- Jähne B, Klinke J and Waas S 1994 Imaging of short ocean wind waves: a critical theoretical review *J. Opt. Soc. Am. A* **11** 2197–209
- Jähne B, Munnich K O, Bosinger R, Dutzi A, Huber W and Libner P 1987 On the parameters influencing air-water gas exchange *J. Geophys. Res.* **92** 1937–49
- Jähne B and Riemer K S 1990 Two-dimensional wave number spectra of small-scale water surface waves *J. Geophys. Res.* **95** 11531–46
- Jähne B and Schultz H 1992 Calibration and accuracy of optical slope measurements for short wind waves *Proc. SPIE Optics of the Air-Sea Interface: Theory and Measurements (San Diego, CA)* vol 1749, pp 222–33
- Jähne B, Waas S and Klinke J 1992 A critical theoretical review of optical techniques for short ocean wave measurements *Proc. SPIE Optics of the Air-Sea Interface: Theory and Measurements (San Diego, CA)* vol 1749, pp 204–15
- Kattawar G W and Adams C N 1989 Stokes vector calculations of the submarine light field in an atmosphere-ocean with scattering according to a Rayleigh phase matrix: effect of interface refractive index on radiance and polarization *Limnol. Oceanogr.* **34** 1453–72
- Keller W C and Gotwols B L 1983 Two-dimensional optical measurement of wave slope *Appl. Opt.* **22** 3476–8
- Klinke J and Jähne B 1995 Measurements of short wind waves during the MBLARI west coast experiment *Air-Water Gas Transfer* ed B Jähne and E C Monahan (Hanau: AEON) pp 165–73
- Lamb H 1945 *Hydrodynamics* (New York: Dover) p 738
- Le Mehaute B and Khangaonkar T 1990 Dynamic interaction of intense rain with water waves *J. Phys. Oceanogr.* **20** 1805–12
- Leykin I A and Rosenberg A D 1984 Sea-tower measurements of wind-wave spectra in the Caspian Sea *J. Phys. Oceanogr.* **14** 168–76
- Liu H and Lin J 1982 On the spectra of high frequency wind waves *J. Fluid Mech.* **123** 165–85
- Liu Y and Voss K J 1997 Polarized radiance distribution measurements of skylight: II. Experiment and data *Appl. Opt.* **36** 8753–64
- Schultz H 1994 Retrieving shape information from multiple images of a specular surface *IEEE Trans. Pattern Anal. Mach. Intell.* **16** 195–201
- Schultz H 1996 Shape reconstruction from multiple images of the ocean surface *Photogramm. Eng. Remote Sens.* **62** 93–9
- Siddiqui M H K, Loewen M R, Asher W E and Jessup A T 2004 Coherent structures beneath wind waves and their influence on air-water gas transfer *J. Geophys. Res.* **109** C03024 doi:10.1029/2002JC001559
- Stillwell D and Pilon R O 1974 Directional spectra of surface waves from photographs *J. Geophys. Res.* **79** 1277–84
- Stokes G G 1852 On the composition and resolution of streams of polarized light from different sources *Trans. Cambridge Phil. Soc.* **9** 399–416
- Sun J, Burns S P, Vandemark D, Donelan M A, Mahrt L, Crawford T L, Herbers T H C, Crescenti G H and French J R 2005 Measurement of directional wave spectra using aircraft laser altimeters *J. Atmos. Oceanic Technol.* **22** 869–85
- Tang S and Wu J 1992 Suppression of wind-generated ripples by natural films: a laboratory study *J. Geophys. Res.* **97** 5301–6
- Voss K J and Liu Y 1997 Polarized radiance distribution measurements of skylight: I. System description and characterization *Appl. Opt.* **36** 6083–94
- Waterman T H 1981 Polarization sensitivity *Handbook of Sensory Physiology, Vision of Invertebrates* ed H J Altrum (Berlin: Springer) pp 283–463
- Wei Y and Wu J 1992 *In situ* measurements of surface tension, wave damping, and wind properties modified by natural films *J. Geophys. Res.* **97** 5307–13
- Wolff L B 1987 Surface orientation from polarization images *SPIE Proc. Optics Illumination and Image Sensing for Machine Vision II* vol 850, pp 110–21
- Wolff L B and Boulton T E 1991 Constraining object features using a polarization reflectance model *IEEE Trans. Pattern Anal. Mach. Intell.* **13** 635–57
- Yang Z, Tang S and Wu J 1997 An experimental study of rain effects on fine structures of wind waves *J. Phys. Oceanogr.* **27** 419–30
- Zappa C J, Asher W E and Jessup A T 2001 Microscale wave breaking and air-water gas transfer *J. Geophys. Res.* **106** 9385–91
- Zappa C J, Asher W E, Jessup A T, Klinke J and Long S R 2004 Microbreaking and the enhancement of air-water transfer velocity *J. Geophys. Res.* **109** C08S16 doi:10.1029/2003JC001897